



Numerical simulation of tunneling through arbitrary potential barriers applied on MIM and MIIM rectenna diodes

Tarek M Abdolkader¹ , Ahmed Shaker²  and A N M Alahmadi³

¹ Department of Basic Engineering Sciences, Faculty of Engineering, Benha University, Egypt, (now with Umm Al-Qura University, Makkah, Saudi Arabia)

² Department of Engineering Physics and Mathematics, Faculty of Engineering, Ain Shams University, Cairo, Egypt

³ Department of Electrical Engineering, Umm Al-Qura University, Makkah, Saudi Arabia

E-mail: tmhasan@uqu.edu.sa

Received 24 December 2017, revised 26 February 2018

Accepted for publication 12 March 2018

Published 1 May 2018



CrossMark

Abstract

With the continuous miniaturization of electronic devices, quantum-mechanical effects such as tunneling become more effective in many device applications. In this paper, a numerical simulation tool is developed under a MATLAB environment to calculate the tunneling probability and current through an arbitrary potential barrier comparing three different numerical techniques: the finite difference method, transfer matrix method, and transmission line method. For benchmarking, the tool is applied to many case studies such as the rectangular single barrier, rectangular double barrier, and continuous bell-shaped potential barrier, each compared to analytical solutions and giving the dependence of the error on the number of mesh points. In addition, a thorough study of the $J - V$ characteristics of MIM and MIIM diodes, used as rectifiers for rectenna solar cells, is presented and simulations are compared to experimental results showing satisfactory agreement. On the undergraduate level, the tool provides a deeper insight for students to compare numerical techniques used to solve various tunneling problems and helps students to choose a suitable technique for a certain application.

Keywords: finite difference method, transfer matrix method, transmission line method, tunneling, numerical simulation, rectenna solar cell, MIM and MIIM diodes

(Some figures may appear in colour only in the online journal)

1. Introduction

One of the most significant distinctions between classical and modern physics is the tunneling phenomenon, which is considered an essential effect in quantum mechanics. Tunneling refers to the transmission of microscopic particles through any arbitrary barrier with energy less than the barrier height [1–4]. It is usually assumed that the energy of the particle remains constant during the tunneling process.

There are many applications in modern physics and technology where tunneling plays an important role. Some applications include molecular biology [5], scanning tunneling microscopy (STM) [6], and modern electronic devices [7, 8].

Double-barrier structures (DBS) are widely used in various engineering fields [7, 9]. DBS is the basis of the resonant tunneling diode. The tunneling effect is responsible for the N -shaped $J - V$ characteristics and the negative differential resistance [10]. Resonant tunneling through the DBS is also utilized for electromagnetic waves [11].

For simple barriers, analytical expressions may be found in the literature. For instance, the tunneling probability of a rectangular barrier is a standard illustration in many undergraduate textbooks [12, 13]. Extensions for double and triple rectangular barriers have been a subject of thorough study [14]. However, for more complicated structures with multiple barriers, it becomes very difficult to get analytical solutions. The use of numerical methods becomes indispensable to get solutions for such structures. One of the most important approximations used is the Wentzel–Kramers–Brillouin (WKB) method [9]. Unfortunately, this conventional method used to calculate the transmission coefficient fails, for instance, to explain the resonance tunneling phenomena. Additionally, it is difficult to calculate the transmission coefficient in regions where the potential profile changes rapidly which is encountered in many cases such as heterojunction interfaces. Meanwhile, some numerical methods have been developed to solve tunneling problems such as the finite difference method (FDM) [15, 16], transfer matrix method (TMM) [17–20], and transmission line method (TLM) [21, 22].

A recent application of tunneling is the metal–insulator–metal (MIM) and metal–insulator–insulator–metal (MIIM) diodes used as rectifiers in rectenna solar cells. Solar rectenna is becoming one of the most promising solar energy converter technologies that could replace the existing technologies because of its high efficiency at microwave and terahertz frequencies [23]. The rectenna technology is mainly based on a high-frequency antenna to absorb the desired wavelength of the electromagnetic wave and an ultra-high-speed diode that rectifies the output of the antenna into DC. Because of their ability to rectify at high frequencies, MIM and MIIM diodes have been potential candidates for use in rectennas [8].

Using dielectrics with a low barrier height (typically in the order of ~ 0.5 eV) and relatively thin (typically below 4 nm to keep the tunneling current as the primary transport [24]) improves the performance of the MIM and MIIM diodes. With low-barrier MIM and MIIM structures, the WKB approximation is not tailored well [8], so, it is essential to solve the tunneling problem occurring in such devices more accurately, which can be provided only by numerical methods. Moreover, it is vital to predict the behavior of MIM and MIIM diodes before fabrication, which can be attained through the simulation study presented in this work.

In this work, a tool for the numerical calculation of the tunneling probability through an arbitrary potential barrier using FDM, TMM, and TLM is implemented under a MATLAB environment. The tool gives a comparison between these three methods and helps to determine the best method that can be used for the problem at hand. It also gives the error of the numerical simulation results of many of the known potential barriers compared to analytical ones and studies the dependence of this error on the mesh size. Moreover, it can be applied to

calculate the $J - V$ characteristics of MIM and MIIM diodes. A description of the presented tool is provided in appendix A. In addition, the MATLAB codes are given in appendix B so as to facilitate the reproduction of the tool. In this regard, the tool can be used as a virtual lab for teaching quantum tunneling making it easy for students to inspect and visualize numerous tunneling problems using this tool.

The rest of the paper is organized as follows. In section 2, the formulation of the problem is presented showing the method of discretization of Schrödinger equation using three methods: FDM, TMM, and TLM, which are presented in sections 2.1, 2.2, and 2.3, respectively. This section begins with the basic principles to illustrate the building blocks of the numerical solver of the Schrödinger equation showing how to calculate tunneling probability and how to assess the accuracy. It enables students to compare various methods and to gain insight on how different parameters affect the transmission coefficient. Section 3 begins with the simulation results of some case studies used for benchmarking. In addition, the simulation results of MIM and MIIM diodes are analyzed and compared to the experimental results. This latter part is more suitable for post-graduate students and researchers.

2. Problem formulation and methodology

To solve quantum-tunneling problems considering any arbitrary potential barrier, the Schrödinger's time-independent wave equation inside and outside the barrier is solved. The solution is performed by transforming the analytical equation into a system of algebraic equations (in the case of FDM) or into a system of matrix equations (in the case of TMM and TLM) as will be given in detail in the following sections.

The 1D Schrödinger equation with effective mass approximation including space-dependent effective mass can be written as [25]

$$\frac{d}{dx} \left(\frac{\hbar^2}{2m^*} \frac{d\psi}{dx} \right) + (E - U)\psi = 0, \quad (1)$$

where \hbar is the modified Planck constant, m^* is the effective mass of carriers, U is the electric potential energy, E is carrier energy, and ψ is the electron wave function. ψ , U , and m^* are generally space dependent and, consequently, are all functions of position x .

If the left and right boundaries are assumed to be at equilibrium, with uniform potential energy, then, the wave functions within these boundaries are considered as plane waves. The solution starts with assuming a plane wave of unit amplitude, $\exp(ik_L x)$, is injected from the left boundary in the positive x -direction. A portion of this wave, $r \exp(ik_L x)$, is reflected back to the left boundary in the negative x -direction and another portion is transmitted to the other side of the solution domain (the right boundary) in the positive x -direction. If both boundaries are assumed to be perfectly absorbing, then, both boundaries will cause no more reflections, and consequently, the wave function inside the boundaries can be written as [17]

$$\psi_L(x) = \exp(ik_L x) + r \exp(-ik_L x); x < 0, \quad (2a)$$

$$\psi_R(x) = t \exp(ik_R x); x > L, \quad (2b)$$

where

$$k_{L,R} = \sqrt{2m_{L,R}^*(E - U_{L,R})} / \hbar. \quad (3)$$

The effective masses m_L^* and m_R^* , and potential energies U_L and U_R are those found within the left and right boundaries, respectively. For each relevant energy, E , equation (1)

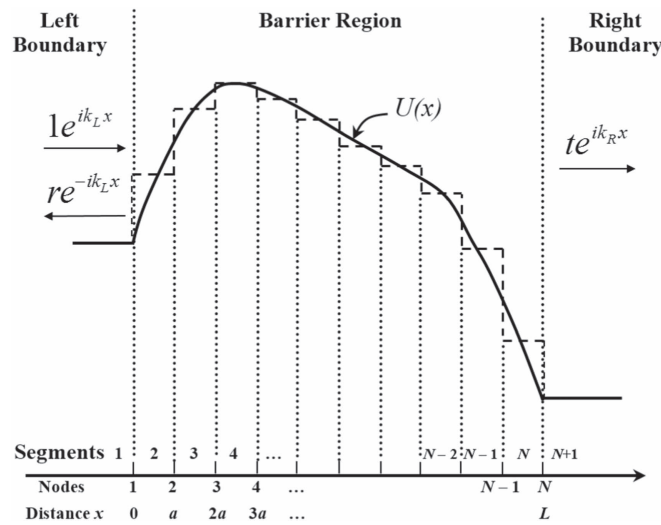


Figure 1. The potential energy distribution, $U(x)$, in a barrier extending from $x = 0$ to $x = L$, along with the mesh used for discretization.

can be solved for $\psi(x)$ subject to the boundary conditions given by equation (2). Upon solution, r and t can be found by knowing the values of $\psi(x)$ at $x = 0$ and $x = L$. The transmission probability through the barrier at a particular energy E , $\tau(E)$, is calculated from the parameter t using [17]

$$\tau(E) = |t|^2 k_R / k_L, \tag{4}$$

with k_L and k_R given by equation (3).

It should be noted that current conservation reads $J_i + J_r = J_t$ or $|J_i| - |J_r| = |J_t|$, where J_i , J_r , and J_t are the incident, reflected, and transmitted currents, respectively. Dividing by $|J_i|$, and knowing that the reflection coefficient $\mathcal{R} = |J_r|/|J_i|$, and the transmission coefficient $\tau = |J_t|/|J_i|$, we can find that $1 - \mathcal{R} = \tau$. From the previous simple equation, it is evident that the reflection and transmission coefficients are related, so, it is sufficient to consider one of them in the calculations.

The numerical solution of the above tunneling problem is usually implemented by the discretization of the Schrödinger equation. This is accomplished by dividing the domain of the solution into small regions (mesh elements) in which some approximation for the wave function is used. The discretization of an arbitrary potential barrier is shown in figure 1. In the following subsections, the basics of the three discretization methods: FDM, TMM, and TLM are explained.

2.1. FDM

The most traditional method of discretization of differential equations is the FDM [16]. The FDM subdivides the simulation domain into small segments which are called mesh elements (see figure 1). Points that separate these segments are called mesh nodes and the unknown variables are defined on these nodes. The derivatives in the differential equation to be solved are replaced by discretized finite difference approximations at each one of the nodes. These approximations may be derived from a truncated Taylor series. If it is assumed that the function $f(x)$ is a continuous, single-valued function with continuous derivatives, then, by

Taylor series expansion we have

$$f(x + \Delta x) = f(x) + \Delta x f'(x) + \frac{\Delta x^2}{2!} f''(x) + \dots, \quad (5)$$

$$f(x - \Delta x) = f(x) - \Delta x f'(x) + \frac{\Delta x^2}{2!} f''(x) - \dots, \quad (6)$$

where Δx is the mesh spacing, which is assumed to be uniform. Truncating each of the above series after the third term, and solving the resulting two equations for $f'(x)$ and $f''(x)$, we get the central finite difference approximations [26]

$$f'(x) = \frac{f(x + \Delta x) - f(x)}{\Delta x}, \quad (7)$$

$$f''(x) = \frac{\frac{f(x + \Delta x) - f(x)}{\Delta x} - \frac{f(x) - f(x - \Delta x)}{\Delta x}}{\Delta x} = \frac{f(x + \Delta x) - 2f(x) + f(x - \Delta x)}{(\Delta x)^2}. \quad (8)$$

Equations (7) and (8) are the cornerstone of FDM. Applying FDM discretization to the Schrödinger equation, we divide the domain into $N - 1$ segments with mesh nodes from 1– N . It should be noted that node 1 is at the interface between the left boundary region and the solution domain. Similarly, node N is located at the interface between the right boundary region and the solution domain. Taking the meshing spacing Δx as a , and using equations (7) and (8), we have for any node i ,

$$\left. \frac{d}{dx} \left(\frac{\psi}{m^*} \right) \right|_i = \frac{\psi_{i+1} - \psi_i}{m_i^* a}, \quad \left. \frac{d}{dx} \left(\frac{\psi}{m^*} \right) \right|_{i-1} = \frac{\psi_i - \psi_{i-1}}{m_{i-1}^* a}, \quad (9)$$

$$\left. \frac{d^2}{dx^2} \left(\frac{\psi}{m^*} \right) \right|_i = \frac{1}{a} \left(\frac{\psi_{i+1} - \psi_i}{m_i^* a} - \frac{\psi_i - \psi_{i-1}}{m_{i-1}^* a} \right), \quad (10)$$

and the Schrödinger equation is written in a discretized form as

$$\eta_{i-1} \psi_{i-1} + [E - U_i - (\eta_i + \eta_{i-1})] \psi_i + \eta_i \psi_{i+1} = 0, \quad (11)$$

where $\eta_i = \hbar^2 / (2a^2 m_i^*)$ and $1 \leq i \leq N$. The boundary conditions are incorporated in the equations of node 1 and node N using equations (2a) and (2b), respectively. Substituting $x = 0$ and $x = -a$ in equation (2a), we get

$$\psi_L(0) = \psi_1 = 1 + r, \quad (12a)$$

$$\psi_L(-a) = \psi_0 = \exp(-ik_L a) + r \exp(ik_L a). \quad (12b)$$

When writing equation (11) at node 1, ψ_0 can be substituted in terms of ψ_1 by eliminating r from equation (12). In a similar approach, substituting $x = L$ and $x = L + a$ in equation (2b), we get

$$\psi_R(L) = \psi_N = t \exp(ik_R L), \quad (13a)$$

$$\psi_R(L + a) = \psi_{N+1} = t \exp(ik_R(L + a)). \quad (13b)$$

Then, when writing equation (11) at node N , ψ_{N+1} can be substituted in terms of ψ_N by eliminating t from equation (13). On eliminating r and t , the equations for nodal points 1 and N are given respectively as

$$[\eta_1 \exp(ik_L a) + E - U_1 - (\eta_1 + \eta_L)] \psi_1 + \eta_1 \psi_2 = 2\eta_L \sin(k_L a), \quad (14a)$$

$$\eta_{N-1}\psi_{N-1} + [E - U_N - (\eta_{N-1} + \eta_R) + \eta_R \exp(ik_R a)]\psi_N = 0, \quad (14b)$$

where η_L and η_R are the values of the parameter η in the left and right boundary regions, respectively. The system of equations (11) and (14) are solved for the wave function values ψ_i at all nodal points including the boundary points. The parameters r and t can then be found from equation (2). Then, the transmission probability is calculated using equation (4). The above procedure is repeated for all relevant energy values to get the transmission probability at all energies. The MATLAB code of the method is given in appendix B.

2.2. TMM

The TMM is a widely used method for quantum device simulation [17–20, 27]. The TMM is based on the assumption that particles enter and exit the system as continuous streams (beams) with amplitudes given by the fixed boundary conditions. The TMM provides efficient simulation of a wide range of structures due to its fast implementation and accurate results [19].

In the TMM, the channel is again divided into small segments of width, a , and the potential within each segment is assumed constant as in the FDM. However, in the TMM, the wave function within each segment n is approximated as a plane wave solution [28],

$$\psi_n(x) = A_n \exp(\alpha_n x) + B_n \exp(-\alpha_n x), \quad (15)$$

where

$$\alpha_n = \sqrt{2m_n^*(U_n - E)}/\hbar, \quad (16)$$

where m_n^* and U_n are the effective mass and potential energy at segment n , respectively.

Applying the continuity conditions of $\psi_n(x)$ and $\frac{d}{dx}\left(\frac{\psi_n}{m_n^*}\right)$ between each two successive segments, we get a series of matrix equations relating A_n and B_n of any segment with those of the preceding segment A_{n-1} and B_{n-1} as follows:

$$\begin{bmatrix} A_{n-1} \\ B_{n-1} \end{bmatrix} = \mathbf{M}^{-1}(n-1, n) \mathbf{M}(n, n) \begin{bmatrix} A_n \\ B_n \end{bmatrix}, \quad (17)$$

where

$$\mathbf{M}(n, l) = \begin{bmatrix} \exp(\alpha_n x_l) & \exp(-\alpha_n x_l) \\ \frac{\alpha_n}{m_n^*} \exp(\alpha_n x_l) & -\frac{\alpha_n}{m_n^*} \exp(-\alpha_n x_l) \end{bmatrix}, \quad (18)$$

with $x_m = (l-1)a$; $m = 1, 2, \dots, N$ cascading all equations relating coefficients of successive segments, we can relate the coefficients of the left boundary to that of the right boundary. This leads to

$$\begin{bmatrix} 1 \\ r \end{bmatrix} = \mathbf{W} \begin{bmatrix} t \\ 0 \end{bmatrix}. \quad (19)$$

The matrix \mathbf{W} is given by

$$\mathbf{W} = \mathbf{M}^{-1}(0, 1) \cdot \mathbf{\Pi} \cdot \mathbf{M}(N, N), \quad (20)$$

where

$$\mathbf{M}(0, 1) = \begin{bmatrix} 1 & 1 \\ \frac{\alpha_L}{m_L^*} & -\frac{\alpha_L}{m_L^*} \end{bmatrix}, \quad (21a)$$

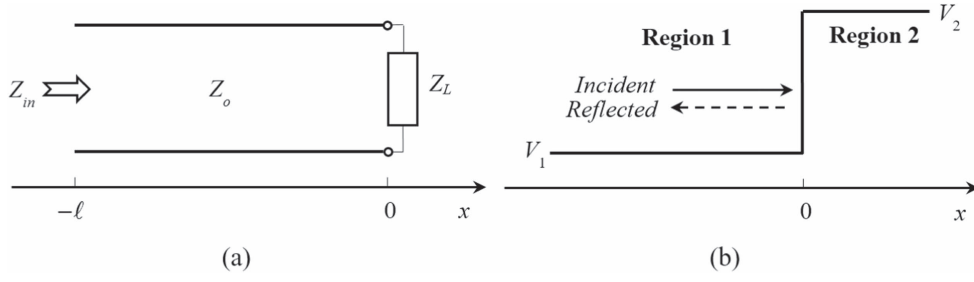


Figure 2. Analogy between (a) a lossy transmission line terminated in an impedance Z_L and (b) a potential step.

$$\mathbf{M}(N, N) = \begin{bmatrix} \exp(\alpha_R L) & \exp(-\alpha_R L) \\ \frac{\alpha_R}{m_R^*} \exp(\alpha_R L) & -\frac{\alpha_R}{m_R^*} \exp(-\alpha_R L) \end{bmatrix}, \quad (21b)$$

$$\mathbf{\Pi} = \mathbf{P}_1 \mathbf{P}_2 \dots \mathbf{P}_{N-1}, \quad (21c)$$

where

$$\mathbf{P}_n = \mathbf{M}(n, n) \mathbf{M}^{-1}(n, n+1). \quad (22)$$

The definitions of $\alpha_{L,R}$ are similar to $k_{L,R}$ in equation (3); $\alpha_{L,R} = \sqrt{2m_{L,R}^*(U_{L,R} - E)}/\hbar$. According to equation (19), r and t can be found in terms of the matrix elements of \mathbf{W} defined in equation (20) as follows:

$$r = \mathbf{W}_{21}/\mathbf{W}_{11} \quad \text{and} \quad t = 1/\mathbf{W}_{11} \quad (23)$$

Once r and t are known, all the coefficients A_n and B_n , and thus the wave function, $\psi_n(x)$, can be found from equation (15). The solution is repeated at different energies in the specified range. The MATLAB code of the method is presented in appendix B.

2.3. TLM

The tunneling probability can be calculated using the analogy between the tunneling barrier and a lossy transmission line. The method is simple and provides an accurate representation to analyze various tunneling problems. Figure 2(a) shows a lossy transmission line terminated in a load impedance Z_L . The length of the transmission line is ℓ along the x -direction. The propagation constant $\gamma = \alpha + j\beta$ is complex. The total current and voltage on the line at any distance x can be written as a sum of incident and reflected waves as follows [22]:

$$I(x) = I_o^+ [\exp(\gamma x) - \Gamma \exp(-\gamma x)], \quad (24a)$$

$$V(x) = I_o^+ Z_o [\exp(\gamma x) + \Gamma \exp(-\gamma x)], \quad (24b)$$

where Z_o is the characteristics impedance, I_o^+ is the incident current amplitude referenced at $x = 0$, and Γ is the reflection coefficient of the load. The total voltage and current at the load are related to the load impedance (at $x = 0$). So, we have

$$Z_L = \frac{V(0)}{I(0)} = Z_o \frac{(1 + \Gamma)}{(1 - \Gamma)}. \quad (25)$$

Then, the reflection coefficient can be extracted as

$$\Gamma = \frac{Z_L - Z_o}{Z_L + Z_o}. \quad (26)$$

The input impedance Z_{in} at a distance ℓ from the load is

$$Z_{in} = \frac{V(-\ell)}{I(-\ell)} = Z_o \frac{Z_L - Z_o \tanh(\gamma\ell)}{Z_o - Z_L \tanh(\gamma\ell)}. \quad (27)$$

To define the quantum-mechanical impedance, let us inspect the propagation of an electron through the boundary between two regions, 1 and 2, across the potential step shown in figure 2(b). Let us assume that an electron energy E is less than the potential height at region 2. In general, the wave function can be written as

$$\psi(x) = A^+ [\exp(\gamma x) - \rho \exp(-\gamma x)], \quad (28)$$

where $\gamma = \alpha + j\beta = j\sqrt{\frac{2m^*}{\hbar^2}(E - V)}$; m^* is the effective mass and ρ is the wave amplitude reflection coefficient. Accordingly, for the potential step, the wave functions in the two regions can be written as

$$\psi_1(x) = A_1^+ [\exp(\gamma_1 x) - \rho \exp(-\gamma_1 x)], \quad x < 0, \quad (29a)$$

$$\psi_2(x) = A_2^+ \exp(\gamma_2 x), \quad x > 0, \quad (29b)$$

where $\gamma_i = j\sqrt{\frac{2m_i^*}{\hbar^2}(E - V_i)}$. Applying the boundary conditions

$$\psi_1(0) = \psi_2(0), \quad (30a)$$

$$\frac{1}{m_1^*} \frac{d\psi_1}{dx} \Big|_{x=0} = \frac{1}{m_2^*} \frac{d\psi_2}{dx} \Big|_{x=0}, \quad (30b)$$

we can get an expression for ρ as

$$\rho = \frac{(\gamma_2/m_2^*) - (\gamma_1/m_1^*)}{(\gamma_2/m_2^*) + (\gamma_1/m_1^*)}. \quad (31)$$

Now, we define a function $\varphi(x)$ as [22]

$$\varphi(x) = \frac{\hbar}{jm^*} \frac{d\psi}{dx} = A^+ Z_o [\exp(\gamma x) + \rho \exp(-\gamma x)], \quad (32)$$

where

$$Z_o = \frac{\gamma \hbar}{jm^*}. \quad (33)$$

If we compare the equations for ψ (equation (28)) and φ (equation (32)) on one side, and the equations for the current I (equation (24a)) and voltage V (equation (24b)) of a transmission line, on the other side, we can see the analogy between them. Consequently, Z_o (given by equation (33)) can be regarded as the characteristic impedance of an analogous transmission line.

To complete this analogy, the ratio of φ and ψ is analogous to the ratio of voltage and current which represents the impedance at any point along the transmission line. Then, at any distance x , we define the quantum-mechanical wave impedance as

$$Z(x) = \frac{\varphi(x)}{\psi(x)}. \quad (34)$$

Table 1. Analogy between the transmission line and quantum mechanics.

Transmission line	Quantum mechanics
$I(x)$	$\psi(x)$
$V(x)$	$\varphi(x) = \frac{\hbar}{jm^*} \frac{d\psi}{dx}$
$\gamma = \alpha + j\beta = \sqrt{(R + j\omega L)(G + j\omega C)}$	$\gamma = \alpha + j\beta = j\sqrt{\frac{2m^*}{\hbar^2}(E - V)}$
$Z_o = \frac{\gamma}{G + j\omega C} = \sqrt{\frac{R + j\omega L}{G + j\omega C}}$	$Z_o = \frac{\gamma\hbar}{jm^*} = \sqrt{\frac{2}{m^*}(E - V)}$
$Z_{in} = Z_o \frac{Z_L - Z_o \tanh(\gamma\ell)}{Z_o - Z_L \tanh(\gamma\ell)}$	$Z_{in} = Z_o \frac{Z_L - Z_o \tanh(\gamma\ell)}{Z_o - Z_L \tanh(\gamma\ell)}$

Thus, finally, the input impedance Z_{in} ($= Z(-\ell)$) can be expressed in terms of Z_L ($= Z(0)$),

$$Z_{in} = Z_o \frac{Z_L - Z_o \tanh(\gamma\ell)}{Z_o - Z_L \tanh(\gamma\ell)}. \quad (35)$$

Table 1 shows the analogous quantities of both the transmission line and quantum mechanics analyses.

The methodology for the calculation of the transmission probability using the TLM is illustrated as follows. Regarding the barrier shown in figure 1, the values of γ and Z_o are calculated, for a given energy E , using constant values for m^* and U in each region (segment), noting that the total number of segments is $N + 1$ as shown. The load Z_L is represented by the characteristic impedance seen from the rightmost section (segment $N + 1$). This means that $Z_L = Z_{o, N+1}$. Next, when looking at point $N - 1$, the input impedance (Z_{N-1}) is calculated using the previously calculated value of Z_L with $Z_o = Z_{o, N}$ and $\ell = a$. Similarly, the input impedance Z_{N-2} is calculated using Z_{N-1} as the load impedance. The process is repeated until the leftmost section is reached (at point 1).

The reflection coefficient ρ for the overall barrier is computed using $Z_{o,1}$ as the characteristic impedance and Z_1 as the load impedance. The quantum-mechanical transmission probability, $T(E)$, is then given by

$$T(E) = 1 - |\rho(E)|^2. \quad (36)$$

The MATLAB code of the method, along with the previous two methods, is presented in appendix B.

3. Results and discussion

The tool could be used to explore a collection of case studies including abruptly changing barriers and continuously changing barriers. In the first case, it will be shown that the TMM and TLM will give more accurate results than the FDM, while in the second case, the FDM is more accurate. The essential difference between the FDM on one side and the TMM and TLM on the other side is that the FDM assumes, in each segment, a linear variation of both potential energy and wave function. On the other hand, the TMM and TLM assume, in each segment, assumes a constant potential energy and a sinusoidal/exponential variation for the wave function. Consequently, for the cases of continuously changing potential energy, the FDM will be superior to other methods as the assumption of staircase potential in the TMM and TLM will be far from the real case. Meanwhile, in abruptly changing potential barriers that may result in a rapidly changing wave function (especially encountered at high energy

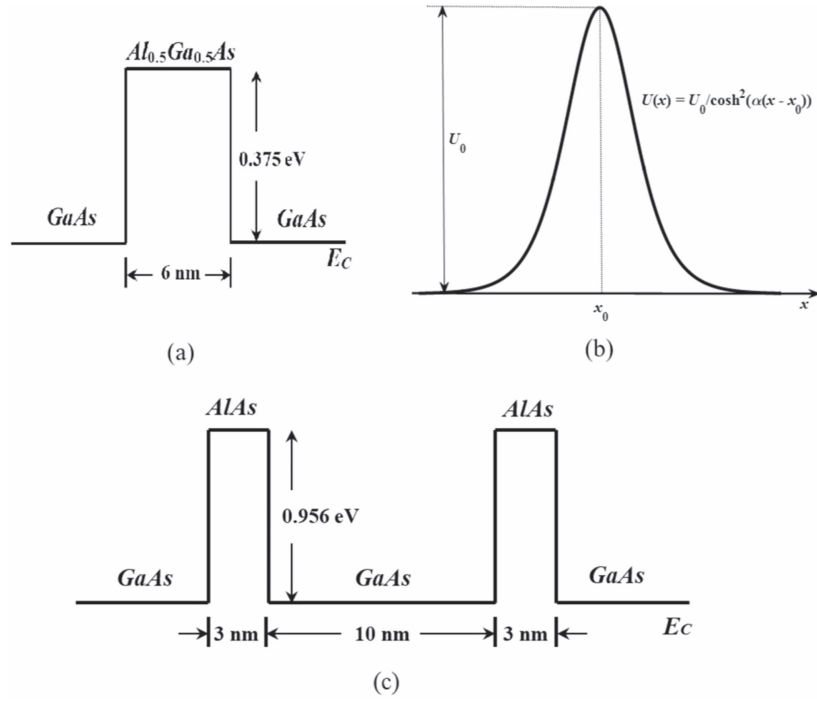


Figure 3. Case studies used for benchmarking. (a) A rectangular barrier composed of AlGaAs sandwiched between two GaAs layers, (b) bell-shaped potential barrier of maximum height U_0 and (c) a double rectangular barrier composed of a GaAs region sandwiched between two AlAs regions.

levels), the TMM and TLM will be more accurate as the wave function in such cases will be far from linearity as assumed by the FDM.

In the first subsection, three case studies, including a rectangular barrier, a bell-shaped potential barrier, and a double barrier composed of a GaAs region sandwiched between two AlAs regions, are presented. The results verify the validity of the tool and effectiveness of each specific discretization method in the simulation of various tunneling phenomena. Moreover, in the second subsection, practical applications for the MIM and MIIM diodes are provided, and the $J - V$ characteristics are compared with experimental results.

3.1. Benchmarking

Here, we provide three case studies for the validation of the presented numerical tool. The case studies used are the rectangular barrier, bell-shaped barrier, and double barrier. The types of barriers under study are shown in figure 3.

For a given number of segments N , the accuracy of a particular method is measured by the error function $f(N)$ [29], which is equal to the norm of difference between the numerical value $T^N(E)$ and the exact value $T_{\text{exact}}(E)$ of the tunneling probability, i.e.

$$f(N) = \|T^N(E) - T_{\text{exact}}\| = \max_E |T^N(E) - T_{\text{exact}}|. \quad (37)$$

This function is used as an error measure for the presented methods.

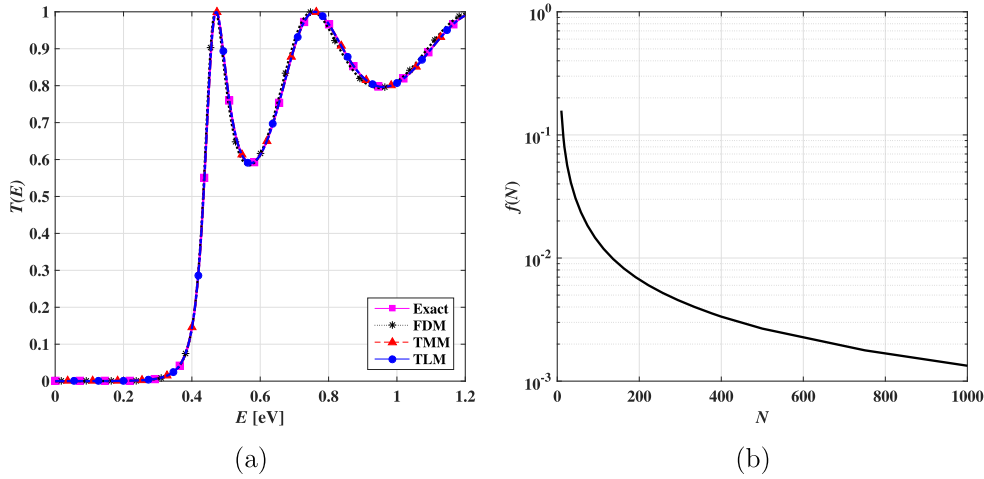


Figure 4. (a) Tunneling probability for the rectangular potential barrier with $N = 50$, (b) error analysis using the norm function $f(N)$ for the rectangular potential barrier for the case of the FDM.

Firstly, we consider the simple case of a rectangular barrier case illustrated in figure 3(a). In this case, the barrier consists of an $\text{Al}_{0.5}\text{Ga}_{0.5}\text{As}$ region embedded between two GaAs boundary regions. The barrier height is $U_o = 0.375$ eV with an effective mass of $m^* = 0.1085 m_0$ and thickness $L = 6$ nm. The effective mass of the boundary regions (GaAs) is $m^* = 0.067 m_0$. The corresponding transmission probability for the FDM, TMM, and TLM along with the exact analytical solution is shown in figure 4(a) for a number of mesh points $N = 50$.

It should be noted that the number of segments used in these simulations does not affect the TMM and TLM results as the error for these methods is independent of N (the TMM and TLM give almost the exact solution for $N = 2$ with a round-off error of $f(N) = 3 \times 10^{-15}$). On the other hand, the simulations for the FDM give a noticeable error when compared to the analytical solution with the accuracy increasing with increasing N . Figure 4(b) shows the error function $f(N)$ for the FDM case, in which, $f(N)$ cannot be lowered below 10^{-3} even for N exceeding 1000.

Next, we consider continuously changing potential barriers, which is called the Pöschl-Teller modified barrier [29], given by the equation

$$U(x) = \frac{U_o}{\cosh^2(\alpha x)}. \quad (38)$$

Figure 3(b) shows the shape of such barrier. Two values of maximum potential energy $U_o = 0.1$ eV and 0.5 eV are considered. For either case, the transmission probability is calculated using the three methods, FDM, TMM and TLM with $N = 100$. The results are given in figure 5(a) along with the exact analytical results as found in [30].

In figure 5(b), the $f(N)$ for the two cases with $U_o = 0.5$ and $U_o = 0.1$ eV is shown. It can be seen that the accuracy in the lower barrier potential case is better than that of the higher potential. Also, it is evident that the FDM solutions are more accurate than the other two methods.

A simple example which illustrates the resonance tunneling phenomena gives a unity transmission probability for particle energy $E > U_o$ and is the double rectangular potential

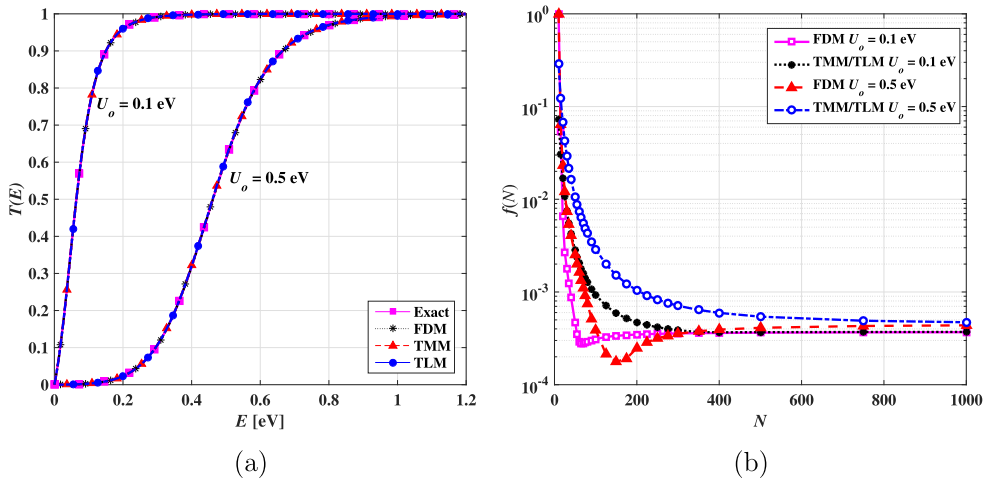


Figure 5. (a) Tunneling probability for the bell-shaped potential barrier for the two values of maximum potential energy $U_o = 0.1$ V, and $U_o = 0.5$ V, both with $N = 100$. The exact solution is also shown for comparison. (b) Error analysis using the norm function $f(N)$ for the bell-shaped potential barrier.

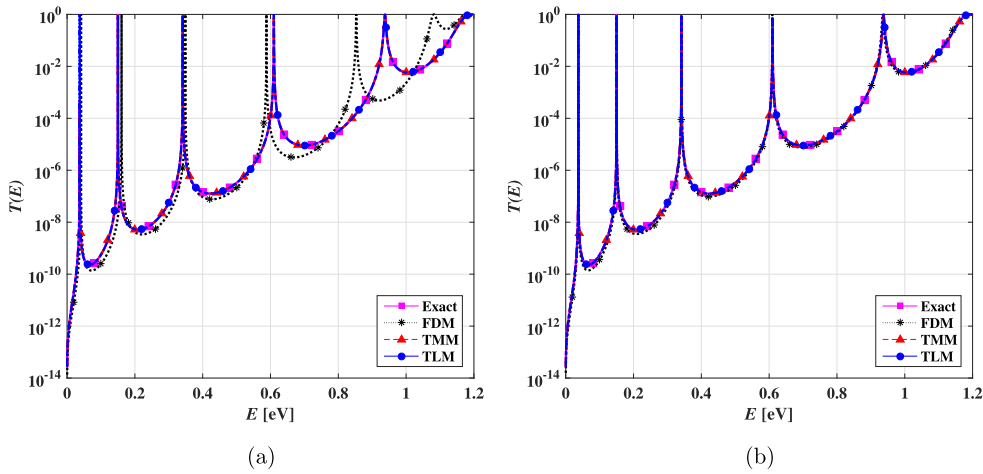


Figure 6. Tunneling probability for the rectangular double potential barrier with (a) $N = 17$ and (b) $N = 97$.

barrier sketched in figure 3(c) similar to the case study in [20]. For each barrier, the barrier width is 3 nm, the well width is 10 nm, and the barrier energy is 0.956 eV.

Simulations are performed for two values of $N = 17$ and $N = 97$ and are shown in figures 6(a) and (b), respectively. There are sharp maxima below 1 eV which can be interpreted as quasi-bound states with narrow energetic bandwidth through which electrons can tunnel.

As can be depicted, from figure 6, the number of segments used does not affect the TMM and TLM results, while the simulations for the FDM give a noticeable error when compared to the analytical solution. Figure 7 shows the error function $f(N)$ for the FDM case, in which

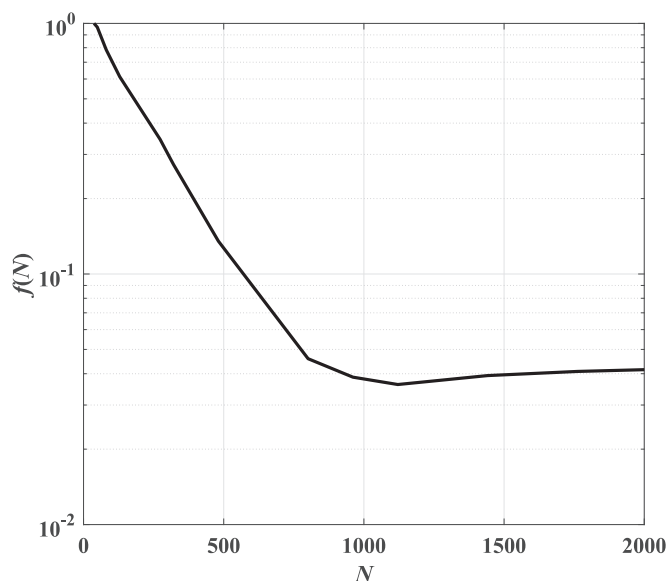


Figure 7. Error analysis using the norm function $f(N)$ for the double rectangular potential barriers for the case of the FDM.

$f(N)$ cannot be lowered below 10^{-2} even for high values of N . Moreover, it can be depicted that at large values of N , the discretization error is decreased as expected but, because of the increased number of calculations, a floating point error starts to dominate and the total error slightly increases.

3.2. MIM and MIIM diodes

MIM diodes are attractive rectifying devices for electronics and energy harvesting applications which are based on tunneling through an insulator layer sandwiched between two metal contacts [31]. The MIM diode used here as a case study (see figure 8(a)) has the following characteristics: NbN is used as the left metal electrode, while Nb is used for the right metal electrode, which, from the experimental point of view, can quickly form a native oxide layer (Nb_2O_5) without forming an unintended interfacial layer. A single 2nm Nb_2O_5 layer is assumed according to the experimental results [32]. The work functions of NbN and Nb are 4.7 eV and 4.33 eV, respectively. The electron affinity of Nb_2O_5 is 4.23 eV while its dielectric constant is 25. In the simulations, the Fermi level energy (at the left of the MIM) is assumed to be $E_F = 10$ eV.

Firstly, the transmission probability of the diode under test is calculated for the TMM (which gives the same results as the TLM). The calculated results are compared to the quantum transmitting boundary method (QTBM) [33] as shown in figure 9. The comparison indicates the effect of the image force. It can be concluded here that the inclusion of the image force is necessary when dealing with such small thicknesses encountered in rectenna diode rectifiers.

Figure 10 shows the comparison of the FDM and TMM in the case of an applied forward voltage of $V = 0.3$ V for different values of N . It can be verified that the FDM is more advantageous for barriers of continuous distribution as stated above.

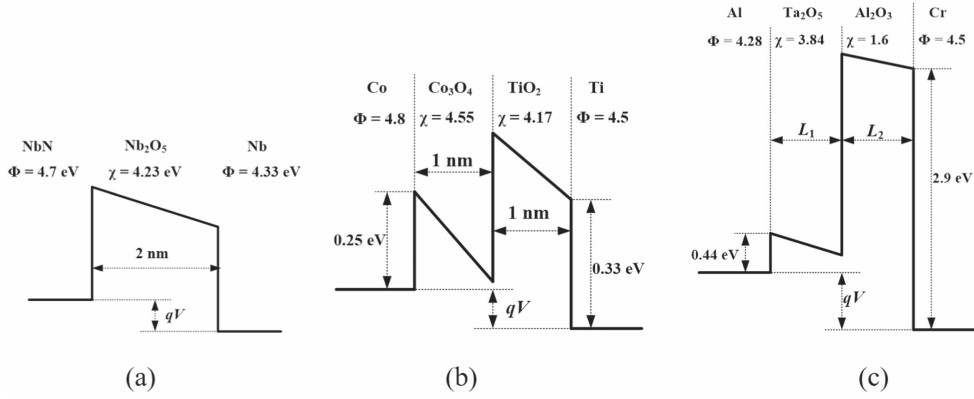


Figure 8. Energy band diagram for the three case studies used in this work: (a) NbN – Nb₂O₅ – Nb MIM diode, (b) Co – Co₃O₄ – TiO₂ – Ti MIIM diode, and (c) Al – Ta₂O₅ – Al₂O₃ – Cr MIIM diode.

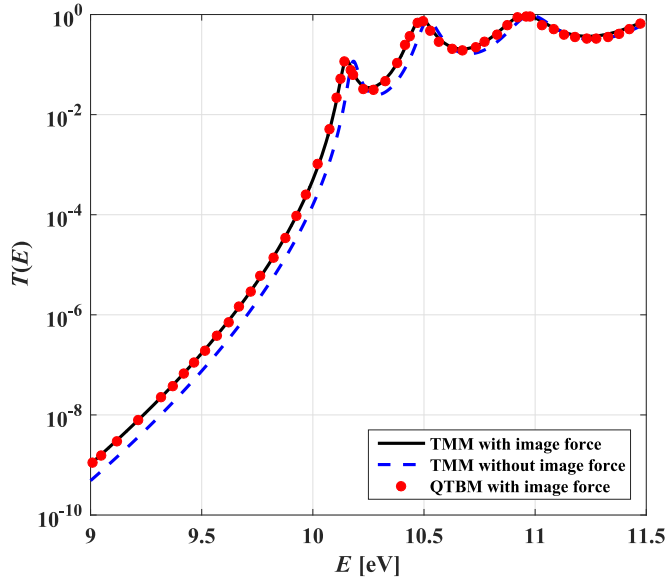


Figure 9. Tunneling probability for an MIM diode showing the effect of image force.

Finally, the current densities of the FDM, using $N = 100$, are calculated and compared with the fabricated MIM diode to validate our simulations. The current is calculated based on the Simmons tunneling model which is valid for MIM structures [34],

$$J(V) = \frac{4\pi m_o e}{h^3} \int_0^\infty T(E_x) dE_x \int_{E_x}^\infty [f_L(E) - f_R(E + eV)] dE, \quad (39)$$

where f_L and f_R are the Fermi–Dirac distribution functions on the left and right metal electrodes, respectively. They are given by

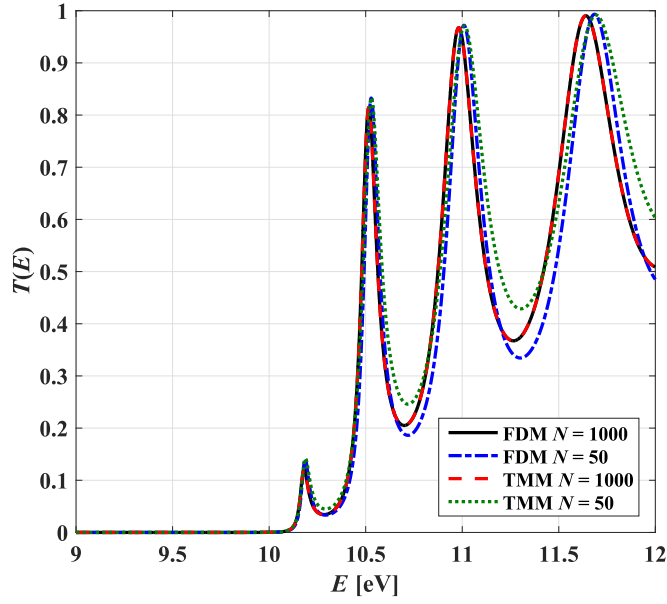


Figure 10. Tunneling probability for an MIM diode for $V = 0.3$ V using the TMM and FDM.

$$f_L(E) = \frac{1}{1 + \exp\left(\frac{E - E_F}{kT}\right)}, \quad (40a)$$

$$f_R(E + eV) = \frac{1}{1 + \exp\left(\frac{E - E_F}{kT}\right)}. \quad (40b)$$

The results of comparing the FDM with the experimental data are presented in figure 11. Two cases are considered: the first case is when the insulator thickness is 2 nm, while in the other case the width is 1.8 nm. It is clear that the results of both cases match well with the experimental data.

An MIIM diode having two insulators with different affinities has superior diode characteristics such as large responsivity, asymmetry, nonlinearity, and high-speed operation compared to the MIM diode [35]. Tunneling through MIIM structures has two mechanisms: (1) step tunneling which occurs when the metal Fermi level aligns with the conduction band of the lower barrier, consequently, the tunnel distance decreases abruptly, (2) resonant tunneling which occurs due to allowed bound states arising in a quantum well formed between the two barriers. When an allowed energy level in the quantum well aligns with the metal Fermi level, a sharp turn-on of the rectifier occurs. The choice of insulator materials, metal work functions, and oxide thicknesses determines the dominant mechanism [35]. With small barrier offsets, step tunneling is the dominant mechanism, while for large barrier offsets, resonant tunneling is more effective.

The first MIIM structure to be studied in this work (see figure 8(b)) consists of a Co metal layer used as a left contact, Co_3O_4 insulator (with a dielectric constant of 13) followed by a TiO_2 insulator (with a dielectric constant of 15) and a Ti metal layer used as the right contact [36]. The metal work functions used are 4.8 and 4.5 eV for the Co and Ti,

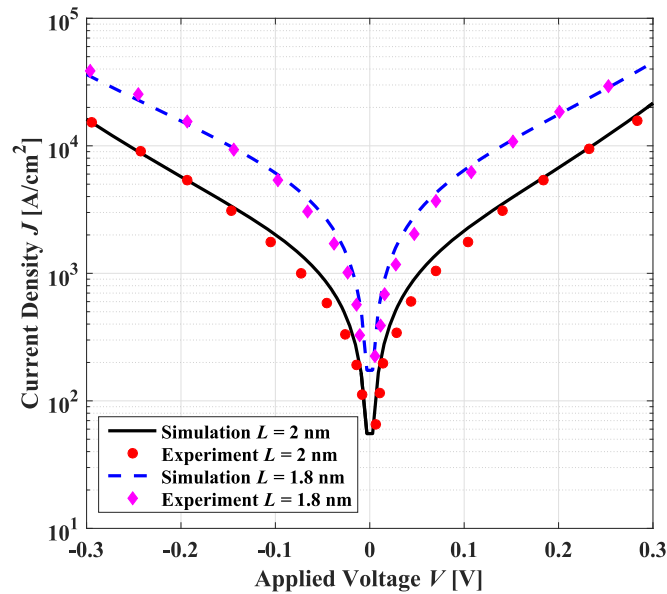


Figure 11. Current density versus applied voltage for fabricated MIM diodes compared with simulation results of FDM using $N = 100$.

respectively [34]. The second MIIM structure is based on an $\text{Al}_2\text{O}_3 - \text{TiO}_2$ system (the dielectric constant of Al_2O_3 is 20 while that of TiO_2 is 10) (see figure 8(c)), for which, the left metal is Al and the right metal is Cr with work functions 4.28 and 4.5eV, respectively [31]. The first MIIM structure illustrates the step tunneling phenomena, while the other shows the resonance tunneling behavior. The difference between the step tunneling and resonance tunneling can be visualized by observing the transmission probability versus energy as explained hereinafter.

Figure 12 shows the tunneling probability in the first MIIM structure at two different voltages 0.3 and 0.5 V. It can be seen from the figure that at both voltages the dominant tunneling mechanism is step tunneling as there is no opportunity for resonance tunneling to occur even for higher voltages. The step tunneling behavior is reflected on the $J - V$ characteristics. The simulated $J - V$ characteristics along with the experimental results are shown in figure 13. The best fit with the experimental results is obtained for affinities of 4.55 and 4.27 eV for the Co_3O_4 and TiO_2 insulators, respectively, which is close to the reported values [36].

The quantum well between the two oxide layers of the MIIM becomes deeper by increasing the thickness of the oxide with a higher dielectric constant [31]. If a relatively high potential is applied to the right electrode, bound states may exist that support resonance tunneling. This can be seen in the second MIIM structure where resonance tunneling is observed clearly as indicated in figure 14. The figure shows the tunneling probability for two cases: at $V \approx 0.3$ V (figure 14(a)) and $V \approx 0.7$ V (figure 14(b)). Also, two oxide (Ta_2O_5) thicknesses are studied. It can be observed that when the oxide thickness increases, the quantum well becomes deeper leading to more bound states. When the bound state energy matches one of the states neighboring the Fermi level on the left side, resonance is maximum.

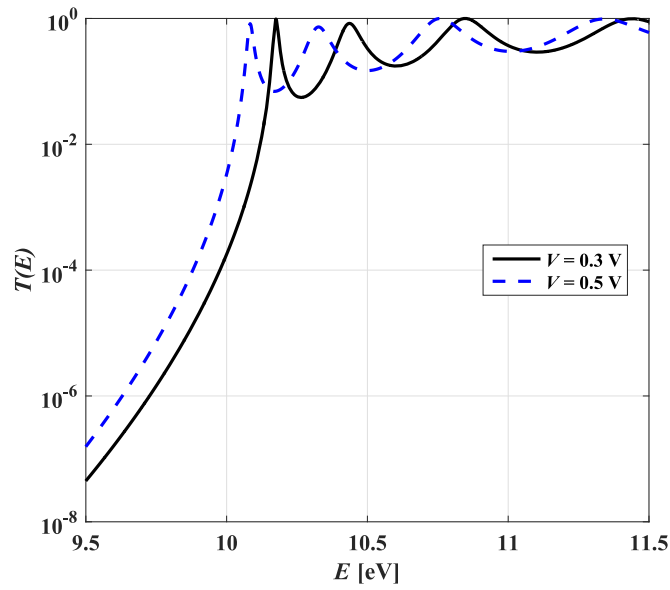


Figure 12. Transmission probability versus energy for the Co – Co₃O₄ – TiO₂ – Ti MIIM system for two different voltages.

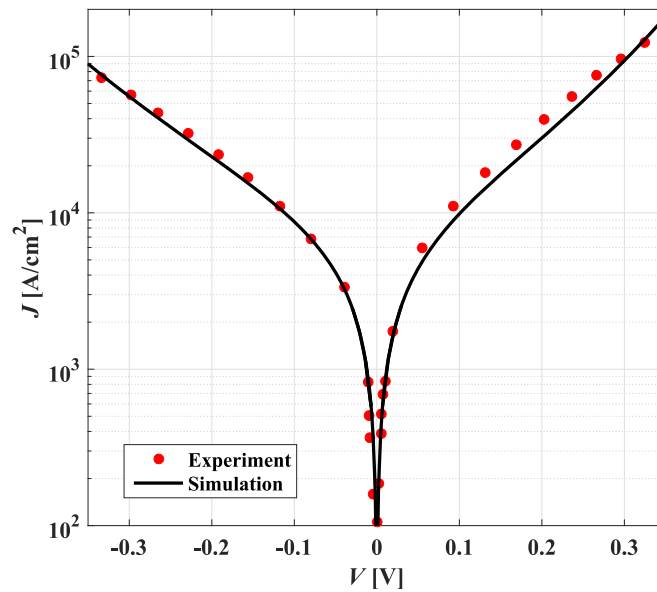


Figure 13. Simulated current density versus applied voltage along with the experimental values for the step tunneling MIIM diode.

If a potential of 0.3 V is applied, a bound state appears for an oxide thickness of 4 nm that is near the Fermi level. Meanwhile, the bound state appearing for the case of 3 nm is still far from the Fermi level at that bias voltage. Therefore, resonance will

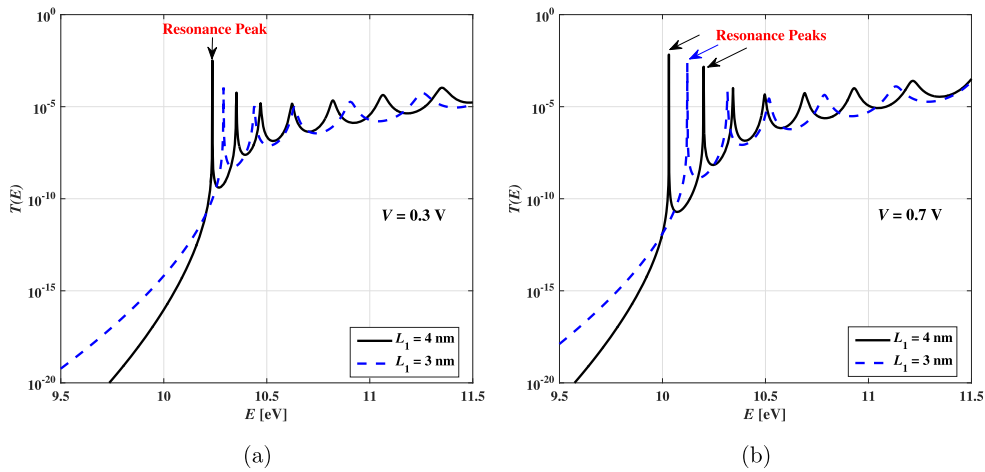


Figure 14. Transmission probability versus energy for the Al – Ta₂O₅ – Al₂O₃ – Cr MIIM system structures: one with Ta₂O₅ insulator thickness $L_1 = 4$ nm and the other for $L_1 = 3$ nm at (a) $V = 0.3$ V and (b) $V = 0.7$ V.

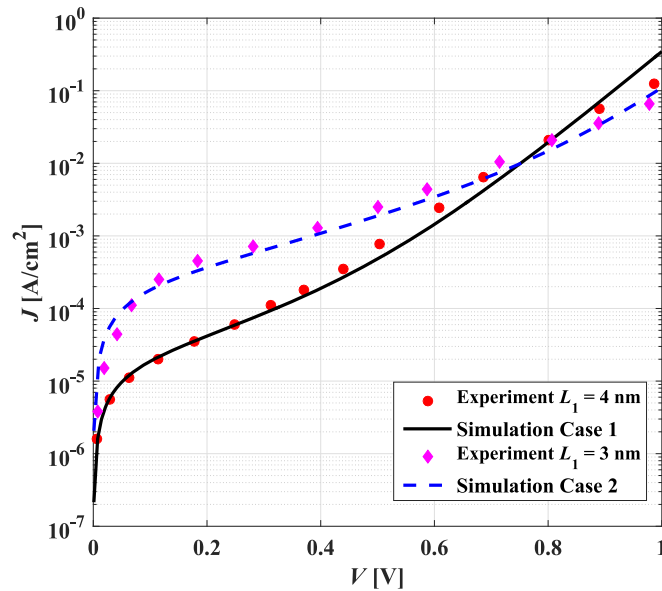


Figure 15. Simulated current density versus applied voltage along with the experimental values for the resonance tunneling MIIM diode.

occur only for the higher oxide thickness. Moreover, for a potential of 0.7 V, there are two bound states (appearing as resonance peaks in the transmission probability as indicated in the figure) corresponding to the higher oxide thickness. One of these bound states is very close to the Fermi level leading to enhanced resonance tunneling. On the other hand, for the lower oxide thickness, there is only one bound state and resonance tunneling will be less effective. From the previous discussion, it can be predicted that the higher oxide

thickness case will give abrupt currents at lower voltages than the lower oxide thickness case.

The simulated $J - V$ characteristics along with the experimental results are shown in figure 15. The best fit with the experimental results is obtained for affinities of 3.84 eV for Al_2O_3 , and 1.6 eV for TiO_2 . The current in the case of $L = 4$ nm starts to increase more steeply above $V \approx 0.3$ V, while it attains this steepness near $V \approx 0.6$ V in the case of $L = 3$ nm. These results are in accordance with the simulated tunneling probability presented above.

4. Conclusion

A numerical simulation tool is developed for the calculation of the transmission probability through any arbitrary potential barrier. The tool is built under a MATLAB environment and incorporates three different discretization methods: FDM, TMM, and TLM. The developed tool is verified by comparing the simulated tunneling probabilities with exact analytical ones for some case studies. It was found that for the cases in which the potential energy changes steeply, the FDM is superior to the other methods as the assumption of staircase potential in the TMM and TLM will be far from the real case. On the other hand, in such cases that may result in a rapidly changing wave function, the TMM and TLM are more accurate as the wave function in such situations will be far from linearity as assumed by the FDM.

Moreover, the tool could be used in the design of the MIM and MIIM diodes encountered in rectenna solar cells by selecting suitable barrier heights and lengths to get the desirable characteristics. The presented work provides undergraduate and post-graduate students with some physical insights into tunneling problems and how to apply numerical methods effectively to study recent tunneling devices.

Acknowledgments

The authors would like to thank the Deanship of Scientific Research at Umm Al-Qura University for the financial support of this project under grant number 43508006.

Appendix A. Tool description

The interface of the developed tool is made user friendly to facilitate changing various parameters such as the analysis type, solution methods, and, physical parameters of the structure at hand. The main menu is shown in figure A1. In this menu, the user can choose one of three analysis types: (1) transmission probability, (2) error analysis, and (3) $I - V$ characteristics. In the first analysis type, the transmission probability ($T(E)$) is plotted versus energy for a certain specified number of mesh points (N). On the other hand, in the second analysis type, the error in transmission probability with respect to the exact analytical solution is plotted versus N at a certain specified energy E . The second analysis type can be chosen only for those structures for which the analytical solution is available. Regarding the last analysis type, $I - V$ characteristics are plotted for MIM or MIIM structures in a predefined voltage range.

In the main menu, the user can also specify the solution method whether it be the FDM, TMM, or TLM. More than one method can be chosen at the same time if a comparison of different methods is needed.

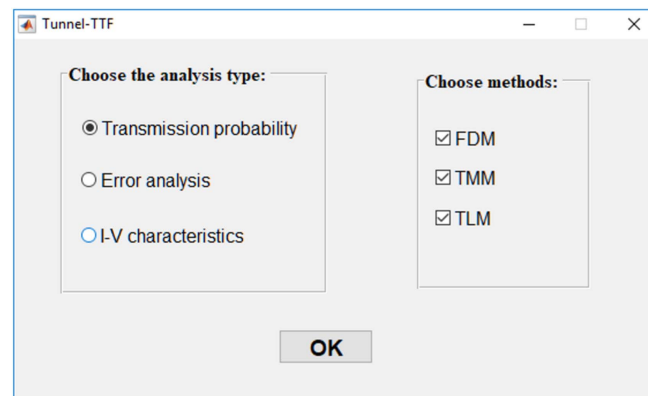


Figure A1. Main menu of the program. The user specifies the analysis type and one or more solution methods.

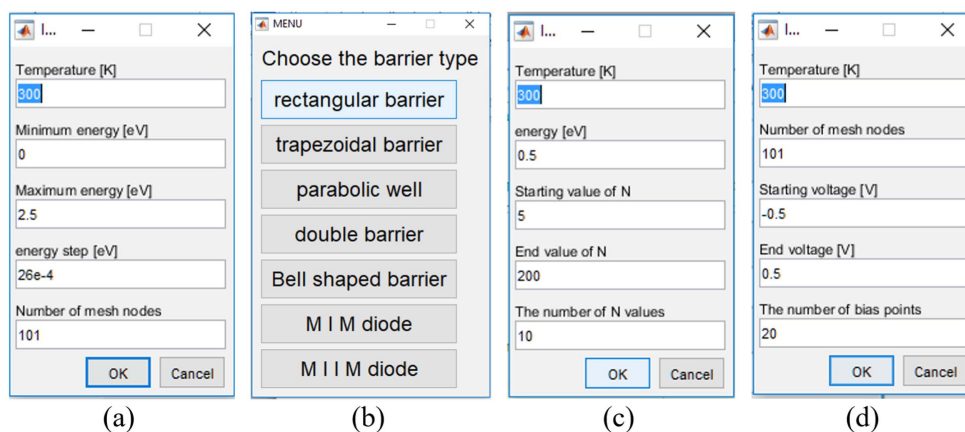


Figure A2. (a) Menu for choosing $T(E)$ plot, (b) menu for choosing the type of structure, (c) menu for choosing the error analysis parameters, and (d) menu for choosing the $I - V$ parameters.

If the user chooses the first analysis method, the menu shown in figure A2(a) will appear. In this menu the user can specify the temperature, minimum energy, maximum energy, energy step, and the number of mesh nodes. After that, a menu for choosing the type of structure to be simulated appears (see figure A2(b)). The tool handles seven different structures: (1) rectangular barrier, (2) trapezoidal barrier, (3) parabolic well, (4) double rectangular barrier, (5) bell-shaped barrier, (6) MIM diode, and (7) MIIM diode. Upon choosing one of these structures, a subsequent menu appears for entering the parameters of this specified structure.

In the main menu, if the user chooses the error analysis type, the menu shown in figure A2(c) appears. In this menu the user specifies the energy at which error is calculated and the range of N for which error is plotted as well as the temperature.

On the other hand, in the main menu, if the user chooses the $I - V$ characteristics, the menu shown in figure A2(d) appears. In this menu the user specifies the voltage range as well as the temperature and number of mesh points. After that a menu for either the MIM or MIIM parameters appears (figure A3).

Input E... — □ ×

Barrier width, L [nm]
2

work function at left, phi_L [eV]
4.7

work function at right, phi_R [eV]
4.33

Affinity, phi [eV]
4.23

Dielectric constant
25

Relative effective mass at boundaries
1

Relative effective mass inside the barrier
1

OK Cancel

Figure A3. Menu for MIM diode parameters.

Appendix B. MATLAB codes

In this appendix the MATLAB code is given for the calculation of the tunneling probability using the three methods: FDM, TMM, and TLM preceded by the definitions of the variables and constants used in the code (sorted in alphabetical order).

B.1. Definitions

α_L the wave number at the left boundary [nm⁻¹].
 α_R the wave number at the right boundary [nm⁻¹].
 E the energy vector [eV]
 E_ref_R the reference energy at the right contact [eV].
 \hbar the modified Planck constant = 1.0545e-34 [J.sec].
 m_{eff_B} the effective mass in the boundary region [Kg].
 m_{eff_mid} the effective mass vector [Kg].
 NE the number of energy values used.
 Np the number of nodal points in the simulated domain.
 Ns the number of segments in the simulated domain.
 q the electronic charge = 1.60218e-19 [C].
 U_b the potential energy vector at nodal points [eV].
 U_B the potential energy vector at the middle of segments [eV].
 w the width of each segment in the mesh [nm].

B.2. FDM Code

```

function [T] = Tunneling__FDM
    Np = Ns + 1;
    mm = [meff__B;meff__mid;meff__B];
    tt = (hbar^2)/(2*mm*1e-18*hat{w}^2*q); %tt is multiplied by 1e-18 to transform from nm-2 to m-2 and
    divided by q to transform from J to eV
    B = zeros(Np,1); %constant vector for solving Schrodinger eq.
    for i = 1:NE
        H = diag(E(i)- Ub - (tt(1:end-1) + tt(2:end))) + diag(tt(2:Np),1) + diag(tt(2:Np),-1);
        H(1,1) = H(1,1) + tt(1)*exp(-alfa__L(i)*w);
        H(Np,Np) = H(Np,Np) + tt(Np+1)*exp(-alfa__R(i)*w);
        B(1) = -2*tt(1)*sinh(alfa__L(i)*w);
        psi = H^-1*B;
        t = psi(Np)*exp(alfa__R(i)*w);
        T(i) = (alfa__R(i)/alfa__L(i))*abs(t)^2; % T is the transmission probability
    end

```

B.3. TMM Code

```

function [T] = Tunneling__TMM
    alfa = zeros(NE,Ns);
    for i = 1:NE
        alfa(i,:) = 1e-9*sqrt(2*q*meff__mid.*(UB-E(i)))/hbar; % nm-1
    end
    % To avoid divide by zero, replace zero entries in alfa by a small number
    alfa(alfa==0)=eps;
    % See details of Mpro function below
    [Mpro11,Mpro12,Mpro21,Mpro22]=Mpro(alfa,meff__mid,w,NE,Ns);
    % We divide here meff__B by 9.10953e-31 just for normalization
    mr = meff__B/9.10953e-31;
    WW11 = mr * exp(alfa__R*w*Ns)/(2*alfa__L).*(alfa__L.*Mpro11(:,1)/mr ...
    + Mpro21(:,1)+alfa__R/mr.*(alfa__L/mr.*Mpro12(:,1)+Mpro22(:,1)));
    t = 1./WW11;
    T = (alfa__R./alfa__L).*abs(t)^2;
    function [pro11,pro12,pro21,pro22]=Mpro(alfa,meff__mid,w,NE,Ns)
        % To evaluate the product of matrices Pi,Pi+1,...PN
        % pro11,pro22 are dimensionless, pro12 is in nm and pro21 is in nm-1
        % Initially we should multiply by identity matrix
        pro11(:,Ns+1) = ones(NE,1);
        pro12(:,Ns+1) = zeros(NE,1);
        pro21(:,Ns+1) = zeros(NE,1);
        pro22(:,Ns+1) = ones(NE,1);
        % loop on different points in the domain starting from right
        for i=Ns:-1:1
            M11 = cosh(alfa(:,i)*w);
            M22 = M11;
            m = meff__mid(i)/9.10953e-31;
            M12 = - m*sinh(alfa(:,i)*w)/alfa(:,i);
            M21 = - alfa(:,i).*sinh(alfa(:,i)*w)/m;

```

(Continued.)

```

pro11(:,i) = M11 .* pro11(:,i+1) + M12 .* pro21(:,i+1);
pro12(:,i) = M11 .* pro12(:,i+1) + M12 .* pro22(:,i+1);
pro21(:,i) = M21 .* pro11(:,i+1) + M22 .* pro21(:,i+1);
pro22(:,i) = M21 .* pro12(:,i+1) + M22 .* pro22(:,i+1);
end

```

B.4. TLM Code

```

function [T] = Tunneling_TLM
% NN is the no. of points in addition to left and right boundary points
NN = Ns+2;
UU = [0;UB;E_ref_R]; % potential energy array used for TLM
mm = [meff_B;meff_mid;meff_B];
gg = zeros(NN,NE);
Zo = zeros(NN,NE);
for i = 1:NE
gg(:,i) = li*(1e-9)*(sqrt(2*q*mm.*(E(i) - UU)/hbar^2)); % nm-1
Zo(:,i) = gg(:,i)*hbar./(li*mm);
end
ZL = Zo(NN,:);
for n = NN-1:-1:2
ZL=Zo(n,:).*((ZL+Zo(n,:).*tanh(gg(n,:)*w))./(Zo(n,:)+ZL.*tanh(gg(n,:)*w)));
end
rho=(ZL-Zo(1,:))./(ZL+Zo(1,:));
T = 1-(abs(rho))^2;

```

ORCID iDs

Tarek M Abdolkader  <https://orcid.org/0000-0002-9885-1502>

Ahmed Shaker  <https://orcid.org/0000-0001-6602-7343>

References

- [1] Wittmann M C, Morgan J T and Bao L 2005 Addressing student models of energy loss in quantum tunnelling *Eur. J. Phys.* **26** 939–50
- [2] Razavy M 2003 *Quantum Theory of Tunneling* (Singapore: World Scientific)
- [3] Ankerhold J 2007 *Quantum Tunneling in Complex Systems: The Semiclassical Approach* (Berlin: Springer Tracts in Modern Physics)
- [4] Takagi S 2002 *Macroscopic Quantum Tunneling* (Cambridge: Cambridge University Press)
- [5] Arndt M, Juffmann T and Vedral V 2009 Quantum physics meets biology *HFSP J.* **3** 386–400
- [6] Magoga M, Archambault F and Cerdá J I 2012 NtSTM: A step forward in scanning tunneling microscopy (STM) simulations *Comput. Phys. Commun.* **183** 1246–9
- [7] Mendez B and Domínguez-Adame F 1994 Numerical study of electron tunneling through heterostructures *Am. J. Phys.* **62** 143–7
- [8] Grover S and Modell G 2011 Applicability of metal/insulator/metal (MIM) diodes to solar rectennas *IEEE J. Photovoltaics* **1** 78–83
- [9] Garg A 2000 Tunnel splittings for one-dimensional potential wells revisited *Am. J. Phys.* **68** 430–7

- [10] Nguyen H S *et al* 2013 Realization of a double-barrier resonant tunneling diode for cavity polaritons *Phys. Rev. Lett.* **110** 236601
- [11] Seo K, Ihm G, Ahn K-H and Lee S 2004 Spin filtering in an electromagnetic structure *J. Appl. Phys.* **95** 7252–4
- [12] Beiser A 2003 *Concepts of Modern Physics* (New York: McGraw-Hill) p 542
- [13] Merzbacher E 1998 *Quantum Mechanics* (New York: Wiley)
- [14] Dutt A and Kar S 2010 Smooth double barriers in quantum mechanics *Am. J. Phys.* **78** 1352–60
- [15] Van der Maelen J F, Granda S G and Velázquez A M 1996 Solving one-dimensional Schrodinger-like equations using a numerical matrix method *Am. J. Phys.* **64** 327–32
- [16] Boykin T B and Klimeck G 2005 The discretized Schrodinger equation for the finite square well and its relationship to solid-state physics *Eur. J. Phys.* **26** 865–81
- [17] Tarek M A 2007 A new approach for numerical simulation of quantum transport in double-gate SOI *Int. J. Numer. Model.* **20** 299–309
- [18] Tarek M A, Hassan H H, Fikry W and Omar O A 2004 Solution of Schrodinger equation in double-gate MOSFETs using transfer matrix method *Electron. Lett.* **40** 1307–8
- [19] Pujol O, Carles R and Philippe J 2014 Quantum propagation and confinement in 1D systems using the transfer-matrix method *Eur. J. Phys.* **35** 035025
- [20] Ando Y and Itoh T 1987 Calculation of transmission tunneling current across arbitrary potential barriers *J. Appl. Phys.* **61** 1497–502
- [21] Anwar A and Jahan M 1995 Traversal time in an asymmetric double-barrier quantum-well structure *IEEE J. Quantum Electron.* **31** 3–7
- [22] Khondker A, Khan M R and Anwar A 1988 Traversal time in an asymmetric double-barrier quantum-well structure *J. Appl. Phys.* **63** 5191–3
- [23] Gadalla M, Abdel-Rahman M and Shamim A 2014 Design, optimization and fabrication of a 28.3 THz nano-rectenna for infrared detection and rectification *Sci. Rep.* **4** 4270
- [24] Simmons J G 1964 Potential barriers and emission-limited current flow between closely spaced parallel metal electrodes *J. Appl. Phys.* **35** 2472–81
- [25] He Y, Cao Z and Shen Q 2005 Analytical formula of the transmission probabilities across arbitrary potential barriers *J. Phys. A: Math. Gen.* **38** 5771–80
- [26] Tarek M A 2005 Modeling and 2D simulation of double-gate SOI devices *PhD Thesis* Ain Shams University
- [27] Gilfoyle G 1999 A new teaching approach to quantum mechanical tunneling *Comput. Phys. Commun.* **121** 573–7
- [28] Kalotas T and Lee A 1991 A new approach to one-dimensional scattering *Am. J. Phys.* **59** 48–52
- [29] Fedirko V, Polyakov S and Zenyuk D 2010 Matrix method for simulating the tunneling transfer, mathematical models and computer simulations *Math. Models Comput. Simul.* **2** 704–13
- [30] Landau L D L D and Lifshitz E M 1977 *Quantum Mechanics: Non-Relativistic Theory* (Oxford: Pergamon)
- [31] Nouredine I N, Sedghi N, Mitrovic I Z and Hall S 2017 Barrier tuning of atomic layer deposited Ta₂O₅ and Al₂O₃ in double dielectric diodes *J. Vac. Sci. Technol. B* **35** 01A117
- [32] Grover S and Moddel G 2012 Engineering the current-voltage characteristics of metal-insulator-metal diodes using double-insulator tunnel barriers *Solid State Electron* **67** 94–9
- [33] Lent C S and Kirkner D J 1990 The quantum transmitting boundary method *J. Appl. Phys.* **67** 6353–9
- [34] Simmons J G 1971 Conduction in thin dielectric films *J. Phys. D: Appl. Phys.* **4** 613
- [35] Weerakkody A D *et al* 2015 Enhanced low voltage nonlinearity in resonant tunneling metal-insulator-insulator-metal nanostructures *J. Microelectron. Eng.* **147** 298–301
- [36] Herner S B, Weerakkody A D, Belkadi A and Moddel G 2017 High performance MIIM diode based on cobalt oxide/titanium oxide *Appl. Phys. Lett.* **110** 223901